solar

MDPI

Article

Investigation of Photovoltaic Module Technologies for Module Integration, Performance Losses, Degradation, and Bifacial–Tandem Architectures

Hasnain Yousuf [1], Rafi Ur Rahman [2], Alamgeer [1], Mengmeng Chu [1], Maha Nur Aida [3], Shurouq Abdulqadir Mohammed [2], Xiaobo Wang [2], Hyejeong Jin [2], Muhammad Quddamah Khokhar [2,*] and Junsin Yi [2,4,*]

[1] Interdisciplinary Program in Photovoltaic System Engineering, Sungkyunkwan University, Suwon 16419, Gyeonggi-do, Republic of Korea; hasnain20@skku.edu (H.Y.); alamgeer9199@skku.edu (A.); chumeng26@skku.edu (M.C.)

[2] Department of Electrical and Computer Engineering, Sungkyunkwan University, Suwon 16419, Gyeonggi-do, Republic of Korea; rafi27@skku.edu (R.U.R.); shurouq5158@skku.edu (S.A.M.); wxb010723@skku.edu (X.W.); jhj1686@skku.edu (H.J.)

[3] Department of Future Energy Engineering, Sungkyunkwan University, Suwon 16419, Gyeonggi-do, Republic of Korea; mahanura18@skku.edu

[4] College of Information and Communication Engineering, Sungkyunkwan University, Suwon 16419, Gyeonggi-do, Republic of Korea

* Correspondence: quddamah@skku.edu (M.Q.K.); junsin@skku.edu (J.Y.)

Abstract

Photovoltaic module performance is governed by the combined effects of solar-cell architecture, optical packaging, electrical interconnection, irradiance distribution, and reliability. This study develops a comparative module-level framework for PERC, n-TOPCon, heterojunction (HJT), interdigitated-back-contact (IBC), parallel-coupled Si/Si, and III–V/crystalline-silicon configurations. The framework combines experimentally measured solar-cell electrical characteristics and parallel Si/Si performance with a literature-supported assessment of module manufacturing, bifacial operation, qualification, degradation, and diagnostics, together with a quantitative factor-resolved cell-to-module analysis of tandem configurations. At their respective technology-specific maximum-output conditions, the PERC-, TOPCon-, HJT-, and IBC-based parallel Si/Si configurations reached η_{tandem} values of 28.42%, 31.62%, 32.43%, and 32.29%, respectively, under the adopted effective front-plus-rear irradiance basis. When the complete front-plus-rear incident power was considered, the corresponding $\eta_{physical}$ values were 23.45%, 26.08%, 26.85%, and 26.65%. The η_{tandem} values represent performance under the adopted rear-side utilization convention and should not be interpreted as complete total-input efficiencies. Factor-resolved CTM analysis yielded module efficiencies of 30.18%, 27.48%, and 31.16% for the III–V Flex/n-TOPCon, GaAs type-1/n-TOPCon, and GaAs type-2/n-TOPCon configurations, corresponding to absolute CTM reductions of 3.56, 3.24, and 3.68 percentage points. The results demonstrate that module performance cannot be inferred from standalone cell efficiency; irradiance normalization, operating-voltage compatibility, optical coupling, inactive area, spectral transmission, and electrical interconnection must be treated consistently.

Keywords: photovoltaic module; cell-to-module loss; PERC; TOPCon; HJT; IBC; bifacial photovoltaics; parallel Si/Si configuration; III–V/Si tandem; module reliability; degradation

Check for updates

Academic Editor: Igor F. Perepichka

Received: 12 July 2026
Revised: 10 August 2026
Accepted: 26 August 2026
Published: 8 September 2026

Copyright: © 2026 by the authors. Licensee MDPI, Basel, Switzerland. This article is an open access article distributed under the terms and conditions of the Creative Commons Attribution (CC BY) license.

1. Introduction

Continuous improvements in crystalline-silicon and multijunction solar-cell efficiency have increased the importance of preserving cell-level performance after module integration. The transition from an individual cell to an encapsulated module introduces front-surface reflection, glass and encapsulant absorption, metallization shading, inactive-area loss, cell mismatch, ribbon resistance, contact resistance, and temperature nonuniformity. These mechanisms can reduce rated module power even when high-efficiency cells are used. Conversely, antireflective glass, refractive-index matching, optical redirection, and light recapture can produce measurable CTM gains. Quantitative separation of these optical, electrical, geometrical, and mismatch contributions is therefore necessary for reliable module-power prediction [1–4].

The magnitude and origin of module-level losses depend strongly on solar-cell architecture. PERC, TOPCon, HJT, and IBC cells differ in their passivation structures, contact arrangements, front-grid shading, transparent-conductive-oxide absorption, rear-side response, operating voltage, and compatible interconnection conditions. TOPCon cells employ an ultrathin tunnel oxide and doped polycrystalline-silicon passivating contact, while HJT cells use amorphous-silicon passivation layers and transparent conductive oxides. IBC and heterojunction-back-contact designs remove front-grid shading but introduce rear-contact alignment and lateral-current-transport requirements [5–7]. These structural differences directly affect optical, resistive, and thermal losses during module fabrication and operation.

Recent progress toward the practical efficiency limit of crystalline-silicon photovoltaics has relied on the simultaneous suppression of bulk and interface recombination, improvement of carrier-selective contacts, reduction in optical losses, and minimization of series resistance. High-efficiency silicon heterojunction and back-contact devices further demonstrate that contact selectivity, interface quality, lateral carrier transport, and metallization design must be optimized together rather than treated as independent factors [8–12].

Bifacial and tandem configurations introduce additional module-level variables. In bifacial operation, rear-side photocurrent depends on albedo, mounting height, tilt, row spacing, structural shading, irradiance nonuniformity, and cell bifaciality. Experimental bifacial-rating and mismatch studies have shown that front and rear irradiance conditions must be declared explicitly and that nonuniform rear illumination can produce measurable electrical losses [13,14]. Validated system-level investigations have additionally demonstrated that bifacial energy gain is strongly influenced by ground reflectance, module elevation, geographic location, tracking configuration, and the spatial distribution of rear-side irradiance [15–17]. Parallel-coupled Si/Si configurations operate through current addition at a common voltage and therefore require operating-voltage compatibility between the coupled cells. In contrast, III–V/Si and perovskite/Si tandems use spectral division between a wide-bandgap top device and a lower-bandgap silicon bottom device [18–26].

Tandem module performance depends not only on the independently measured efficiencies of the component cells but also on top-cell spectral transmission, transparent-electrode absorption, refractive-index mismatch, optical adhesives, terminal configuration, and current or voltage matching. Comparative studies of two-terminal, three-terminal, and four-terminal silicon-based tandem configurations have shown that interconnection topology, optical transmission, subcell spectral response, and current or voltage matching can substantially influence achievable cell- and module-level performance [27–30]. Experimental tandem studies have demonstrated that interface passivation, refractive-index engineering, and optoelectronic coupling strongly influence the final device and module performance [21–26]. In a mechanically stacked III–V/Si configuration, the silicon bottom cell must be evaluated under the spectrum transmitted through the top device rather

than under an independent full one-sun spectrum [19]. Mechanically stacked bifacial III–V/Si devices further require consistent treatment of top-cell transmission, bottom-cell rear illumination, spectral albedo, and the electrical extraction configuration [31].

Previous studies have generally investigated CTM loss, bifacial energy yield, accelerated degradation, infrared fault detection, and tandem optical coupling as separate research problems. Direct comparison remains difficult because different area definitions, irradiance denominators, spectral conditions, rear-side weighting factors, and electrical-connection assumptions are often used [1–4,13,14]. In particular, η_{tandem}, calculated using the effective irradiance basis $G_{front} + \varphi G_{rear}$, is not directly interchangeable with $\eta_{physical}$, which is calculated using the complete front-plus-rear incident power, $G_{front} + G_{rear}$. A consistent module-level framework is therefore required to distinguish irradiance normalization, physical input power, electrical coupling, spectral filtering, CTM loss, and reliability behavior.

1.1. Objectives and Original Contribution

The objective of this study is to establish a consistent module-level framework for comparing silicon and tandem photovoltaic technologies. The investigation has four aims: (i) to relate PERC, TOPCon, HJT, and IBC cell architectures to manufacturing and module-integration requirements; (ii) to compare the characteristic power profiles of tilted, horizontal, vertical east–west, and dual-axis-tracked bifacial configurations; (iii) to experimentally evaluate the voltage-resolved performance of parallel-coupled Si/Si assemblies; and (iv) to quantify the geometrical, optical-loss, optical-gain, and electrical-loss contributions associated with III–V/n-TOPCon cell-to-module conversion. Reliability, qualification, degradation, and infrared diagnostics are included as an evidence-based module assessment framework.

The principal contribution is the separation of normalized bifacial efficiency from physical total-input efficiency and the application of a common CTM accounting basis to conventional silicon, parallel Si/Si, and III–V/Si module configurations. The experimental parallel Si/Si results and the factor-resolved III–V/n-TOPCon CTM results are reported together with their respective irradiance conditions, input assumptions, normalization bases, and evaluation procedures. These results should be interpreted as comparative research outcomes rather than certification-grade module power ratings.

1.2. Performance Definitions

The maximum-power conversion efficiency was calculated using Equation (1), where P_{max} is the measured or calculated maximum electrical power, G is the incident irradiance, and A is the stated active or aperture area. Unless otherwise specified, standard test conditions correspond to the AM1.5G reference spectrum, an irradiance of 1000 W m^{-2}, and a device temperature of 25 °C.

$$\eta = \frac{P_{max}}{G \times A} \times 100 \quad (1)$$

The CTM power ratio and the corresponding CTM loss were calculated using Equations (2) and (3), following established factor-resolved CTM approaches [1–4].

$$CTM_{power} = \frac{P_{module,max}}{\sum P_{cell,max}} \quad (2)$$

$$L_{CTM} = \left(1 - CTM_{power}\right) \times 100 \quad (3)$$

A positive L_{CTM} value denotes module-level power reduction, whereas a negative value denotes CTM gain. For bifacial or separately illuminated configurations, the equivalent and physical irradiance bases were distinguished using Equations (4) and (5).

$$G_{eq} = G_{front} + \varphi G_{rear} \tag{4}$$

$$G_{total} = G_{front} + G_{rear} \tag{5}$$

Here, φ is the effective rear-side utilization factor adopted for the η_{tandem} calculation. The tandem efficiency, η_{tandem}, and physical total-input efficiency, $\eta_{physical}$, were calculated using Equations (6) and (7), respectively.

$$\eta_{tandem} = \frac{P_{max}}{A\left(G_{front} + \varphi G_{rear}\right)} \times 100 \tag{6}$$

$$\eta_{physical} = \frac{P_{max}}{A\left(G_{front} + G_{rear}\right)} \times 100 \tag{7}$$

The coefficient φ represents the effective fraction of rear irradiance included in the adopted η_{tandem} calculation. In the present analysis, φ was back-calculated to reproduce the reported maximum-power densities and original η_{tandem} values rather than obtained from an independent bifaciality measurement. The resulting values were 0.475 for PERC, 0.387 for TOPCon, 0.398 for HJT, and 0.389 for IBC. Accordingly, φ should not be interpreted as an independently measured bifaciality factor. The η_{tandem} values should therefore be regarded as convention-dependent comparative metrics calculated using the effective irradiance $G_{front} + \varphi G_{rear}$. In contrast, $\eta_{physical}$ was calculated independently using the complete incident irradiance $G_{front} + G_{rear}$, without rear-side weighting, and was used for complete incident-power accounting and energy-conservation assessment. The η_{tandem} values retain the original tandem-analysis basis, whereas $\eta_{physical}$ provides the corresponding complete-input efficiency.

2. Materials and Methods

2.1. Study Scope and Evidence Basis

This study combines experimental electrical measurements, factor-resolved CTM analysis, and literature-supported module interpretation. The electrical characteristics of the investigated PERC, TOPCon, HJT, and IBC solar cells and the corresponding parallel Si/Si performance were experimentally evaluated under the stated front- and rear-side irradiance conditions. The measured electrical data were analyzed using the common-voltage current-addition relationship and the efficiency definitions described in Sections 1.2 and 2.4. The III–V/n-TOPCon cell-to-module performance was evaluated using a factor-resolved procedure in which sequential geometrical, optical-loss, optical-gain, and electrical-loss contributions were applied to the initial cell efficiencies. Peer-reviewed literature and relevant IEC standards were used to support the interpretation of cell architecture, bifacial operation, terminal configuration, module integration, qualification, degradation, reliability, and diagnostic mechanisms.

The bifacial-orientation curves are normalized comparative profiles intended to illustrate differences in diurnal output shape and rear-irradiance utilization. They are not presented as site-specific annual-energy-yield predictions or certification-grade performance data. The parallel Si/Si electrical results were obtained from experimental measurements and their common-voltage evaluation, whereas the III–V/n-TOPCon results were obtained through the factor-resolved CTM procedure described in Section 2.5. The bifacial-

orientation, reliability, qualification, degradation, and diagnostic frameworks synthesize comparative trends and mechanisms reported in the cited literature and should not be interpreted as a complete certification campaign. All quantitative results should therefore be interpreted according to the assumptions, irradiance conditions, normalization conventions, input parameters, and evaluation procedures stated in the corresponding sections.

Scope and Interpretation

Figure 1 presents representative photovoltaic cell architectures and module-integration pathways. Figure 2 classifies directly deposited and mechanically stacked tandem photovoltaic architectures according to their terminal configurations. Figure 3 compares characteristic bifacial-module orientations and normalized output profiles. Figure 4 summarizes photovoltaic-module degradation mechanisms, reliability relationships, failure modes, and qualification procedures. Figure 5 presents infrared-thermography-based module diagnostics and field-observed thermal anomalies. Figure 6 presents the quantitative parallel Si/Si tandem and III–V/n-TOPCon cell-to-module analyses. The numerical results should be interpreted according to the assumptions, irradiance bases, and calculation procedures stated in the corresponding sections.

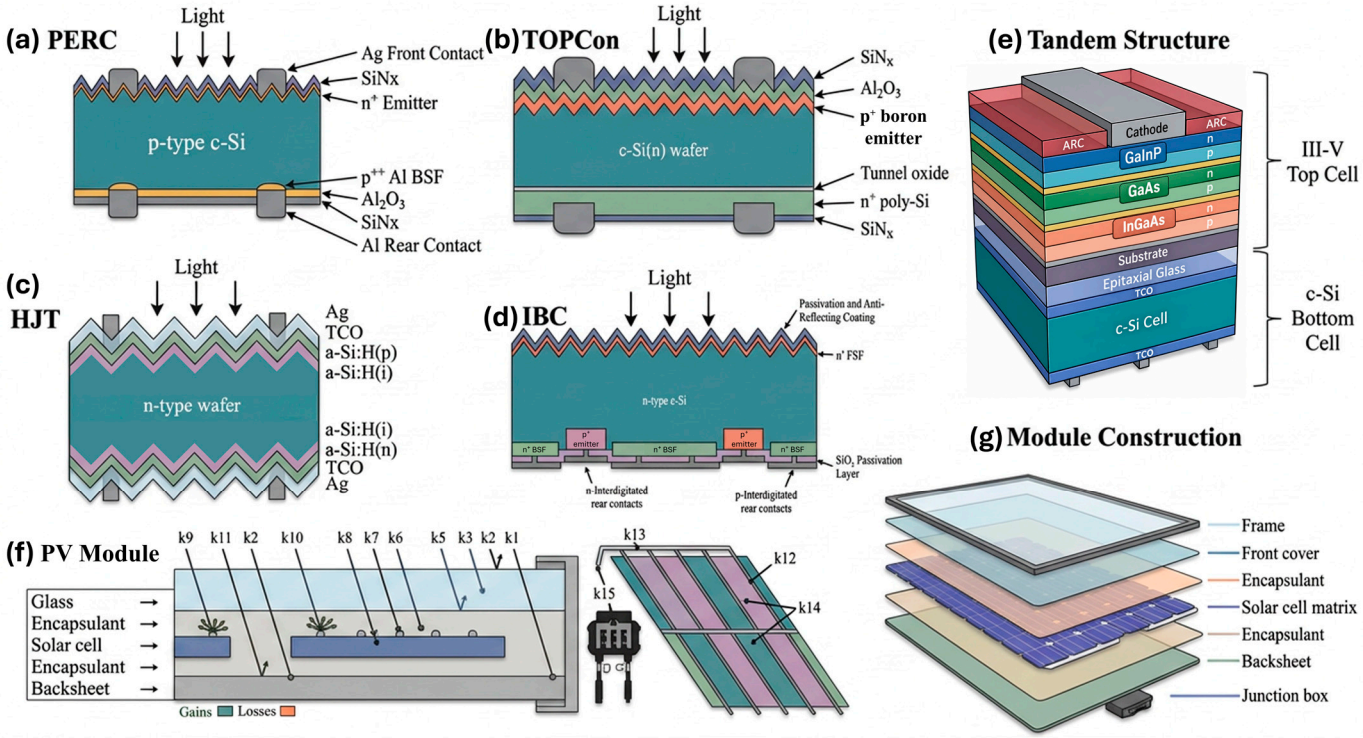


Figure 1. Representative photovoltaic cell architectures and module-integration pathways: (**a**) PERC, (**b**) n-TOPCon, (**c**) HJT, (**d**) IBC, (**e**) mechanically stacked III–V/c-Si configuration, (**f**) principal cell-to-module conversion factors, and (**g**) exploded photovoltaic module construction.

2.2. Cell Architectures and Module Integration

The investigated technology set includes p-type PERC, n-type TOPCon, HJT, IBC, mechanically stacked III–V/c-Si, and bifacial module configurations. Their representative device structures and module-integration pathways are shown in Figure 1. TOPCon employs a tunnel-oxide/polycrystalline-silicon passivating contact, and its module integration is influenced by passivating-contact formation, emitter configuration, metallization, and rear-side optical management [5,32–34]. HJT uses amorphous-silicon passivation layers and transparent conductive oxides; consequently, low-temperature metallization and contact/TCO compatibility are important for preserving cell-level performance during module

integration [6,7,35]. IBC transfers both polarities to the rear surface, eliminating front-grid shading but increasing the importance of rear-contact geometry, alignment, metallization design, and lateral current transport [6,36]. Tandem integration introduces additional requirements associated with spectral filtering, transparent electrodes, bonding, optical interlayers, and terminal configuration [18–31].

Figure 2 classifies the principal tandem photovoltaic architectures according to the integration method and electrical-terminal configuration. Directly deposited architectures include monolithic two-terminal tandems, thin-film tandems, and three-terminal structures formed on silicon. Mechanically stacked configurations use physically separate top and bottom cells and may employ three-terminal, four-terminal, or voltage-matched two-terminal connections. The selected configuration determines the requirements for current matching, voltage matching, optical transmission, bonding-layer design, and independent electrical extraction [18–26].

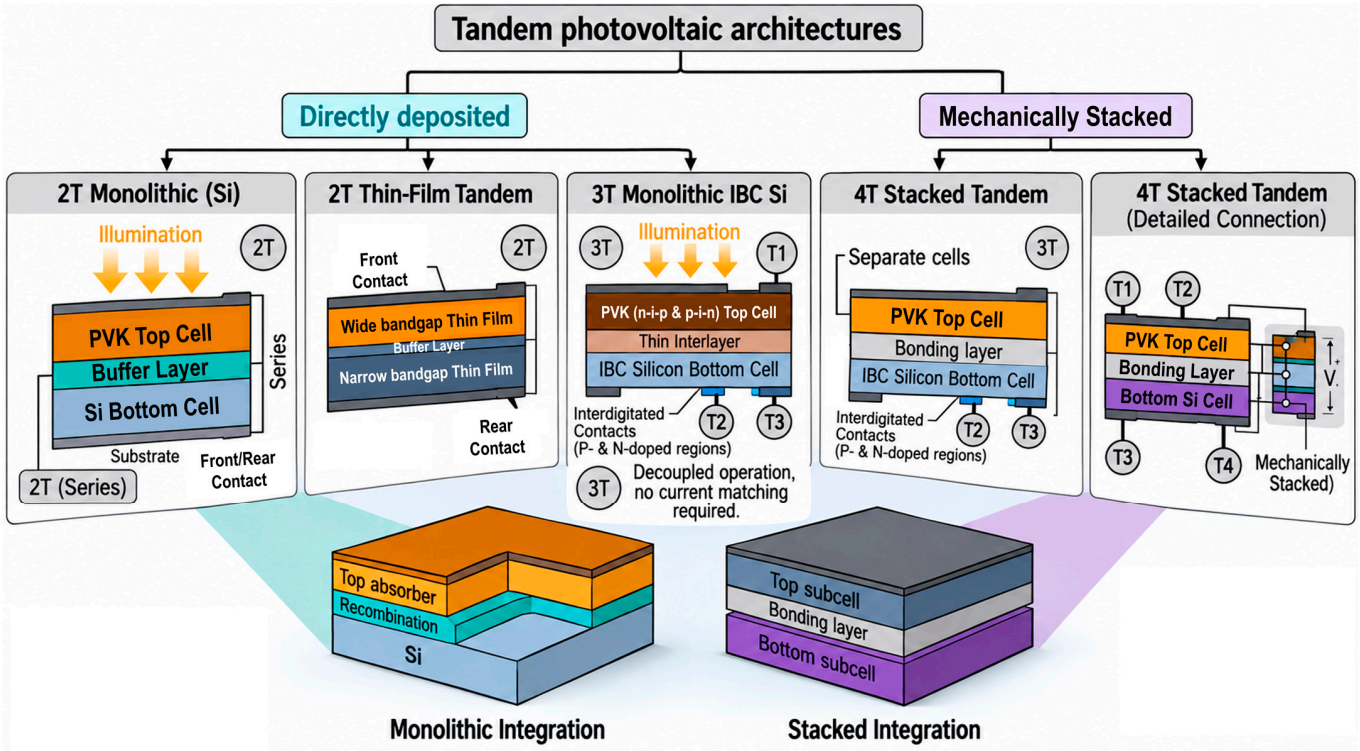


Figure 2. Classification of tandem photovoltaic architectures according to integration and terminal configuration: directly deposited two-terminal monolithic tandems, two-terminal thin-film tandems, three-terminal tandems on silicon, mechanically stacked three-terminal configurations, and four-terminal or voltage-matched two-terminal configurations.

The principal module-level advantages, critical risks, and priority controls for the investigated technology classes are summarized in Table 1. The TOPCon and HJT controls listed in Table 1 reflect the importance of passivating-contact formation, emitter design, firing compatibility, low-temperature metallization, and contact/TCO stability during cell-to-module integration [32–35].

Table 1. Module-level advantages, critical risks, and priority controls for the investigated photovoltaic technologies.

Technology	Module-Level Advantage	Critical Module Risk	Priority Control
PERC	Mature manufacturing and supply chain	LID/LeTID, PID, and rear-contact recombination	Hydrogen management, PID-resistant packaging, and stable firing
TOPCon	High voltage and compatibility with much of the PERC production flow	Contact damage, metallization loss, and rear optical sensitivity	Firing/contact optimization and rear-side optical design
HJT	High V_{oc}, favorable temperature coefficient, and high bifaciality	Low-temperature interconnection and TCO/contact durability	Low-temperature metallization, moisture barriers, and TCO stability
IBC	No front-grid shading and high packing potential	Rear alignment, localized thermal stress, and inspection complexity	Back-contact layout, adhesive reliability, and rear-side inspection
Bifacial	Additional energy from rear irradiance	Site-dependent rating and rear-irradiance mismatch	Declared albedo, height, spacing, and front/rear measurement basis
Tandem	Area-efficiency potential beyond single-junction silicon	Spectral mismatch, optical interlayers, and top-cell stability	Transparent interfaces, terminal design, spectral testing, and edge sealing

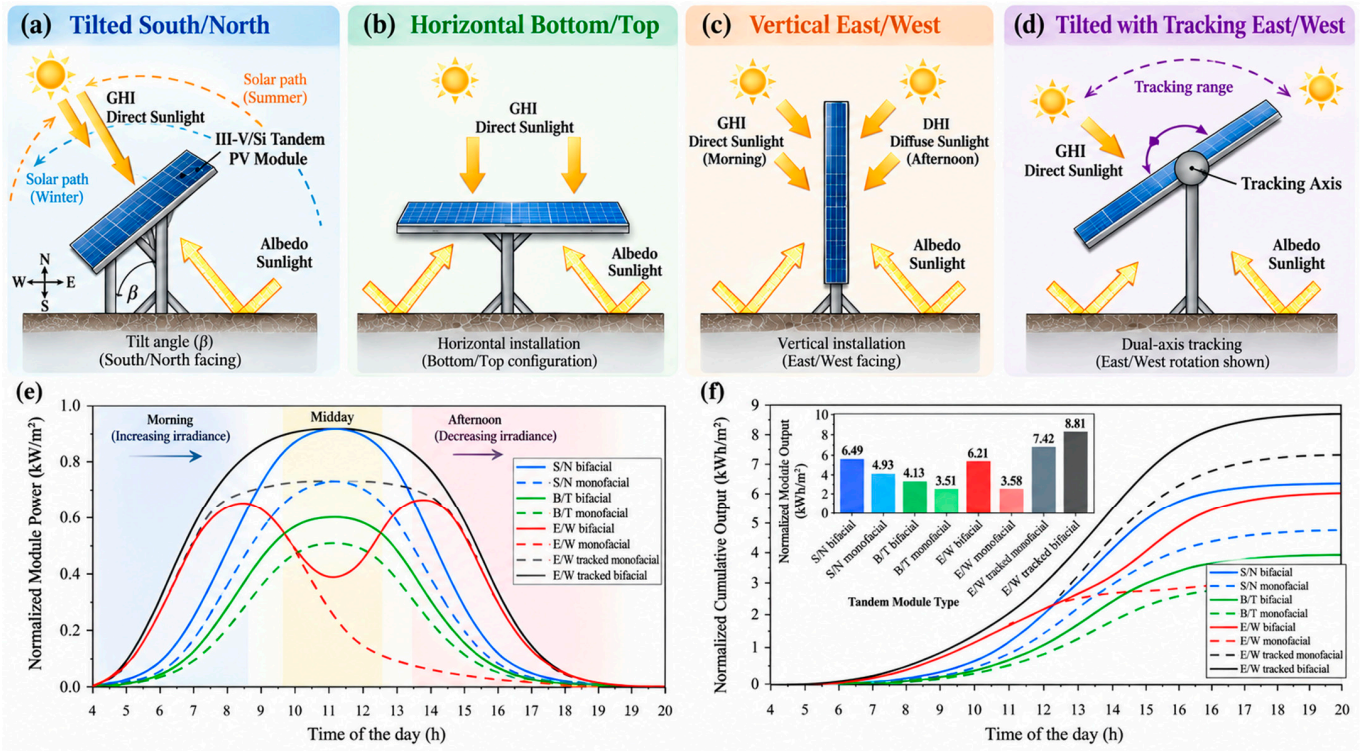


Figure 3. Comparative bifacial module configurations and output profiles: (**a**) tilted south/north-facing configuration, (**b**) horizontal bottom/top-facing configuration, (**c**) vertical east/west-facing configuration, (**d**) tilted dual-axis-tracked east/west-facing configuration, (**e**) normalized diurnal power profiles, and (**f**) normalized cumulative output.

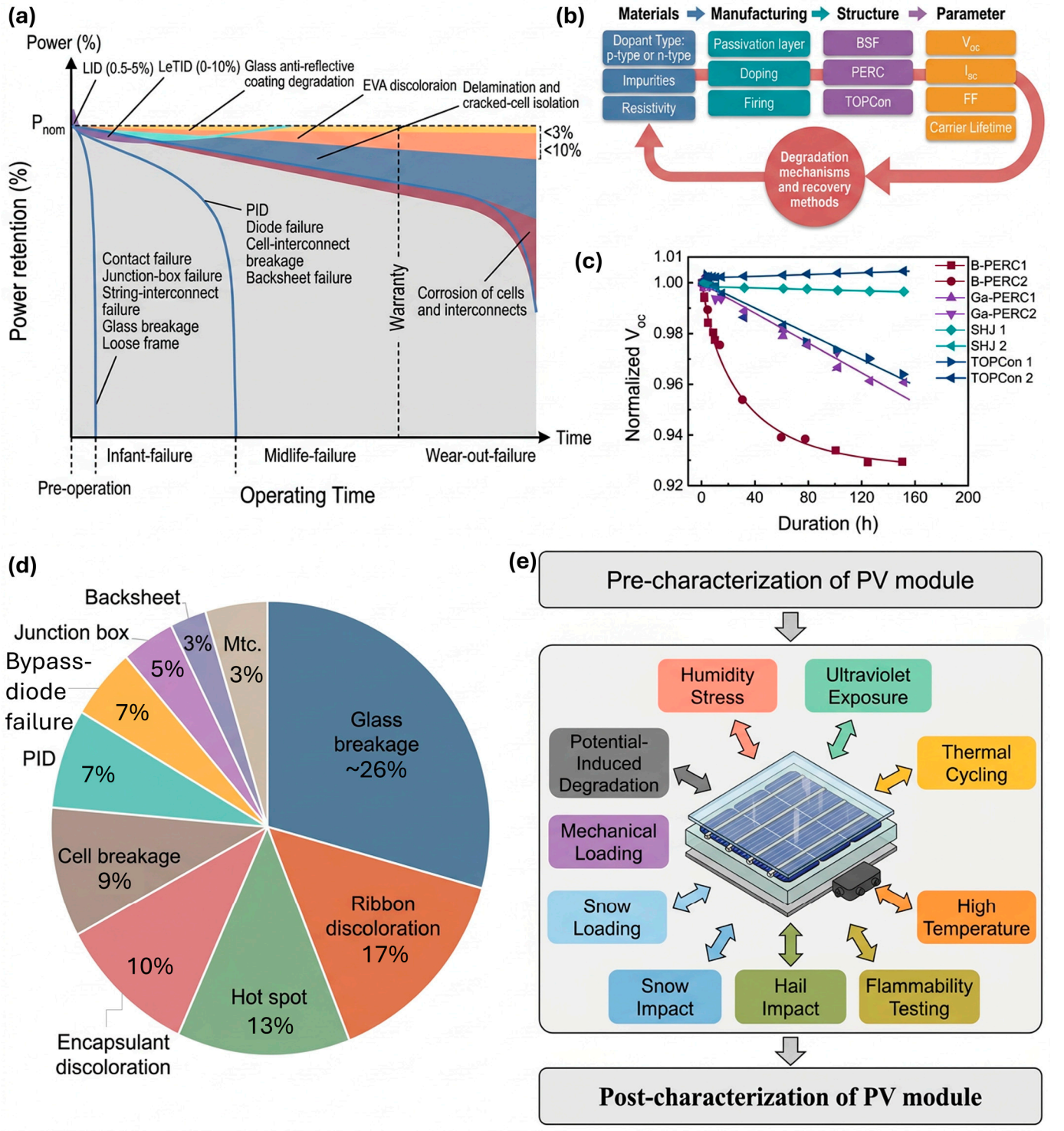


Figure 4. Photovoltaic module reliability and degradation assessment framework: (**a**) representative power-retention stages and degradation mechanisms, (**b**) relationships among materials, manufacturing processes, module structures, and electrical parameters, (**c**) normalized V_{oc} trajectories for PERC, SHJ/HJT, and TOPCon technologies, (**d**) distribution of photovoltaic module failure modes, and (**e**) qualification and pre- and post-characterization workflow. The crack-propagation, PID, and degradation trajectories shown in this figure should be interpreted as technology- and stress-condition-dependent trends rather than universal quantitative degradation rates.

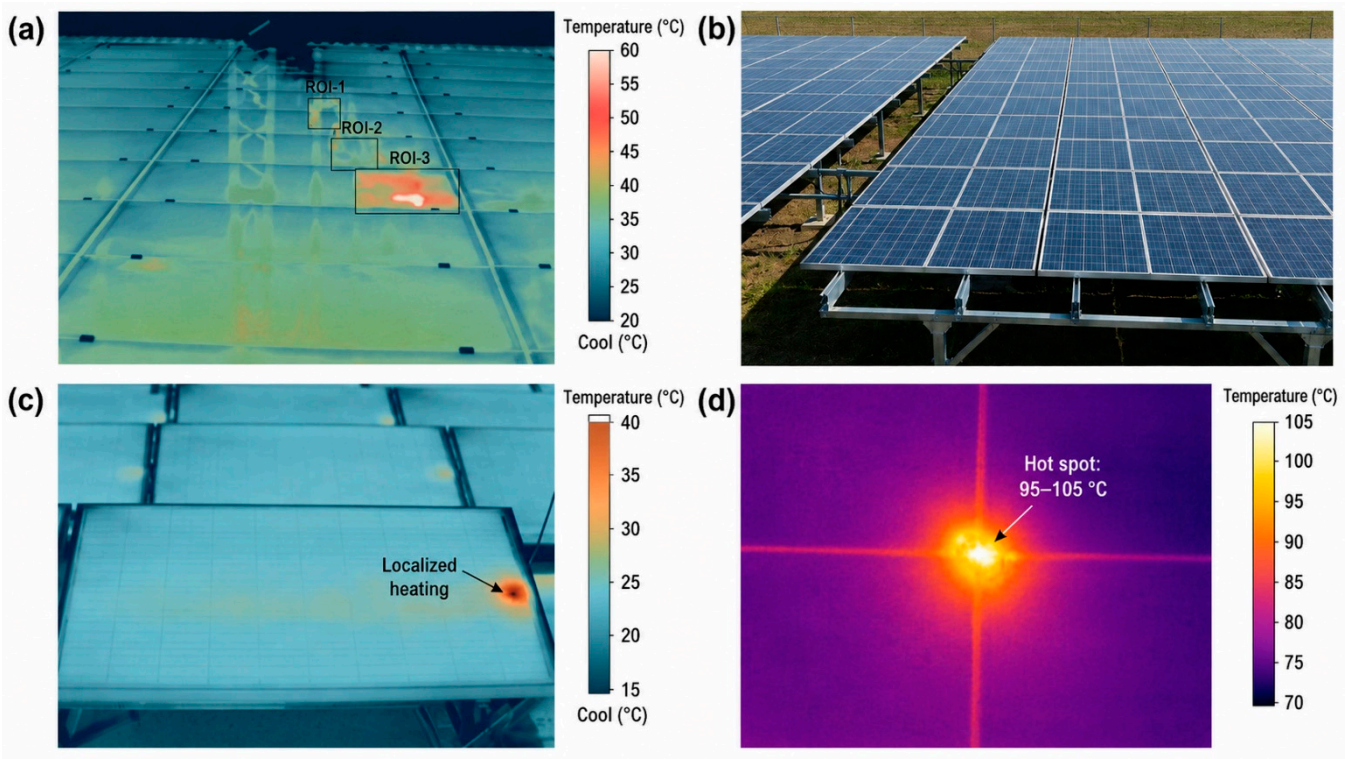


Figure 5. Infrared thermography and field inspection of photovoltaic modules: (**a**) thermal image showing localized temperature anomalies within a field-installed photovoltaic array, (**b**) corresponding photographic image of the inspected array, (**c**) localized module heating associated with a potential electrical or interconnection anomaly, and (**d**) severe localized hot-spot behavior. Infrared observations should be interpreted together with module operating conditions, irradiance, current–voltage measurements, electroluminescence imaging, and visual inspection because similar thermal anomalies may originate from different electrical, mechanical, or interconnection defects.

2.3. Bifacial Orientation Comparison

Four representative bifacial module configurations were compared: tilted south/north-facing, horizontal bottom/top-facing, vertical east/west-facing, and dual-axis-tracked east/west-facing modules. The comparison was intended to illustrate characteristic differences in normalized diurnal output rather than to predict the absolute energy yield of a specific installation. The qualitative interpretation follows established bifacial-rating and irradiance-mismatch studies [13,14,37]. Global horizontal irradiance may be expressed as $GHI = DNI \cos \theta z + DHI$, where DNI is the direct normal irradiance, DHI is the diffuse horizontal irradiance, and θz is the solar-zenith angle. Rear-side irradiance and the resulting bifacial contribution additionally depend on ground albedo, mounting height, module tilt, row spacing, structural shading, tracking strategy, and the spatial uniformity of reflected irradiance. Because no site-specific meteorological dataset or standardized installation geometry was applied, the curves are presented only as normalized comparative profiles. Validated bifacial studies have demonstrated that latitude, ground albedo, module elevation, tracker geometry, rear-side shading, and irradiance nonuniformity can materially change both the daily power profile and annual energy gain [15–17].

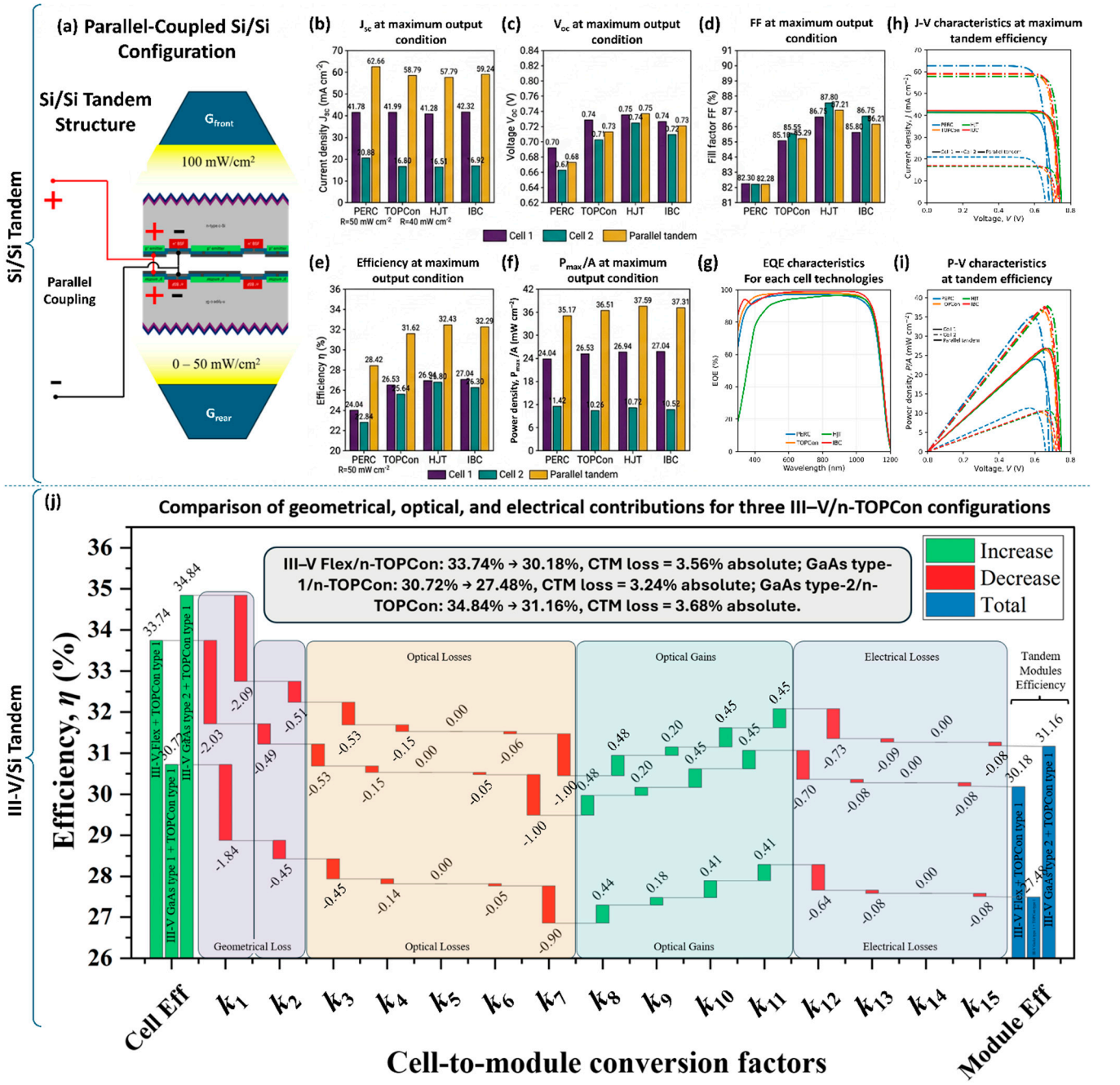


Figure 6. Comparative performance analysis of Si/Si and III–V/Si tandem configurations. The figure is organized into two sections. Section I—Si/Si tandem: (**a**) schematic of the parallel-coupled Si/Si configuration under front-side illumination (G_{front}) and variable rear-side illumination (G_{rear}), (**b**) short-circuit current density, J_{sc}, of Cell 1, Cell 2, and the parallel-coupled configuration, (**c**) corresponding open-circuit voltage, V_{oc}, (**d**) fill factor (FF), (**e**) conversion efficiency, and (**f**) maximum power density, P_{max}/A, evaluated at the respective technology-specific maximum-output conditions for PERC, TOPCon, HJT, and IBC cells, (**g**) external quantum efficiency (EQE) characteristics of the investigated silicon-cell technologies, (**h**) *J*–*V* characteristics of Cell 1, Cell 2, and the corresponding parallel-coupled configurations at the respective maximum-output conditions; and (**i**) corresponding *P*–*V* characteristics. Section II—III–V/Si tandem: (**j**) factor-resolved cell-to-module (CTM) efficiency balance for the III–V Flex/n-TOPCon, GaAs type-1/n-TOPCon, and GaAs type-2/n-TOPCon configurations, showing the sequential contributions of geometrical losses (k_1–k_2), optical losses (k_3–k_7), optical gains (k_8–k_{11}), and electrical losses (k_{12}–k_{15}) to the conversion from cell-level to module-level efficiency.

2.4. Experimental Parallel Si/Si Electrical Evaluation

External quantum efficiency measurements were additionally performed for the investigated PERC, TOPCon, HJT, and IBC silicon solar cells over the wavelength range of 300–1200 nm using a Solar Cell Spectral Response/QE/IPCE Measurement System (Model QEX7, PV Measurements, Inc., Boulder, CO, USA). The EQE system was calibrated using a NIST-traceable calibrated silicon photodiode reference cell (S2281, Hamamatsu Photonics K.K., Hamamatsu, Shizuoka, Japan), and the wavelength-dependent spectral responses of the individual silicon-cell technologies were recorded under short-circuit conditions in photovoltaic mode (0 V bias) using AC lock-in amplification under monochromatic light illumination. The resulting EQE spectra were used to evaluate the wavelength-dependent photocurrent response and to complement the electrical characterization obtained from the J–V measurements.

$$I_{parallel}(V) = I_1\left(V, G_{front}\right) + I_2(V, G_{rear}) \tag{8}$$

$$P_{parallel}(V) = V \times I_{parallel}(V) \tag{9}$$

$$P_{mpp,parallel} = max\left[P_{parallel}(V)\right] \tag{10}$$

$$FF_{parallel} = \frac{P_{mpp,parallel}}{V_{oc,parallel} \times I_{sc,parallel}} \tag{11}$$

The front irradiance was 100 mW cm^{-2}. The rear irradiance at the reported maximum condition was 50 mW cm^{-2} for PERC and 40 mW cm^{-2} for TOPCon, HJT, and IBC. Because these rear inputs differ, the four maxima represent technology-specific operating points rather than a fixed-irradiance head-to-head comparison. The configuration is described here as parallel-coupled Si/Si rather than a conventional spectral tandem because both absorbers have approximately the same bandgap.

2.5. Factor-Resolved III–V/n-TOPCon CTM Analysis

The factor-resolved III–V/n-TOPCon cell-to-module analysis separated the transition from the initial cell efficiency to the resulting module efficiency into ordered geometrical, optical-loss, optical-gain, and electrical-loss contributions. The waterfall representation was generated as a sequential absolute efficiency-point balance.

2.5.1. Optical Bonding-Layer Treatment

The optical effect of the adhesive or bonding interface was included within the optical-loss portion of the factor-resolved CTM sequence. A consistent transmission basis was applied to all three investigated III–V/n-TOPCon configurations, and no additional bonding-layer correction was introduced outside the defined optical-loss contribution. The bonding-layer contribution was therefore incorporated into the cumulative optical-loss balance rather than treated as an independent configuration-specific correction. Because a separate wavelength-dependent bonding-layer transmission dataset was not evaluated, the resulting CTM efficiencies should be interpreted according to this common optical-treatment basis.

2.5.2. Bottom-Cell Spectral Treatment

The n-TOPCon bottom-cell parameters used in the CTM analysis were defined for the spectrum transmitted through the corresponding top-cell stack rather than for an independent full-spectrum one-sun condition. The same spectral-treatment basis was applied consistently to all three investigated configurations. Accordingly, the bottom-cell contribution should be interpreted within the adopted transmitted-spectrum conditions. Because the present comparison does not independently resolve wavelength-dependent transmis-

sion and EQE-integrated current for each configuration, the CTM results are reported as comparative factor-resolved outcomes rather than direct spectral-response measurements.

$$\eta_{module} = \eta_{cell} + \sum_{i=1}^{15} \Delta\eta_i \quad (12)$$

$$\Delta\eta_{CTM} = \eta_{cell} - \eta_{module} \quad (13)$$

The factor positions k_1–k_{15} preserve the ordered CTM sequence shown in Figure 6j. The geometrical-loss factors k_1 and k_2 represent inactive module-margin and cell-spacing areas. Factors k_3–k_7 describe front-cover reflection and absorption, cover-encapsulant interface reflection, encapsulant absorption, and interconnection shading. The optical-gain factors k_8–k_{11} account for refractive-index coupling and the redirection or recapture of light reflected from cell metallization, interconnector ribbons, and module-cover regions. Factors k_{12}–k_{15} describe resistive cell and string interconnection losses, electrical mismatch, and losses associated with module cabling, junction-box components, and bypass diodes. The resulting module efficiency and total CTM reduction were determined using Equations (12) and (13), respectively. The definitions, physical origins, sign conventions, and absolute efficiency contributions of the individual factors are summarized in Table 2. The displayed $\Delta\eta$ values are rounded to two decimal places; therefore, small differences may occur between their arithmetic sum and the final efficiencies calculated using unrounded factor values. This ordered-factor approach is consistent with established CTM methodologies [1–4].

Table 2. Definition, physical origin, sign convention, and absolute efficiency contribution of the k_1–k_{15} CTM factors.

Factor	CTM Category	Physical Meaning	Sign	Flex/ n-TOPCon Δη	GaAs Type-1/ n-TOPCon Δη	GaAs Type-2/ n-TOPCon Δη
k_1	Geometrical loss	Module-margin inactive area	–	−2.03	−1.84	−2.09
k_2	Geometrical loss	Inactive spacing between cells and strings	–	−0.49	−0.45	−0.51
k_3	Optical loss	Reflection of incident light at the front-cover interface	–	−0.53	−0.45	−0.53
k_4	Optical loss	Parasitic absorption in the front cover	–	−0.15	−0.14	−0.15
k_5	Optical loss	Reflection at the cover–encapsulant interface	–	0.00	0.00	0.00
k_6	Optical loss	Parasitic absorption in the encapsulation material	–	−0.05	−0.05	−0.06
k_7	Optical loss	Shading of the active cell area by interconnector ribbons	–	−1.00	−0.90	−1.00
k_8	Optical gain	Reduced cell-surface reflection through cell–encapsulant refractive-index coupling	+	+0.48	+0.44	+0.48
k_9	Optical gain	Redirection of light reflected from the cell fingers toward the active cell area	+	+0.20	+0.18	+0.20

Table 2. *Cont.*

Factor	CTM Category	Physical Meaning	Sign	Flex/ n-TOPCon Δη	GaAs Type-1/ n-TOPCon Δη	GaAs Type-2/ n-TOPCon Δη
k_{10}	Optical gain	Redirection of light reflected from interconnector ribbons toward the active cell area	+	+0.45	+0.41	+0.45
k_{11}	Optical gain	Internal cover or rear-layer reflection returning light from cell-spacing regions to the cells	+	+0.45	+0.41	+0.45
k_{12}	Electrical loss	Resistive loss in cell-interconnection ribbons	−	−0.70	−0.64	−0.73
k_{13}	Electrical loss	Resistive loss in string interconnections	−	−0.08	−0.08	−0.09
k_{14}	Electrical loss	Electrical mismatch caused by variations among cells or cell strings	−	0.00	0.00	0.00
k_{15}	Electrical loss	Electrical loss in module cabling, junction-box components, and bypass diodes	−	−0.08	−0.08	−0.08

Note: The Δη values listed in Table 2 correspond to the factor values displayed in Figure 6j and are expressed as absolute efficiency changes in percentage points. Because the final module efficiencies were calculated using unrounded intermediate values, summing the displayed two-decimal Δη values may produce minor differences of approximately 0.02–0.05 percentage points relative to the final total CTM reductions calculated using the unrounded intermediate values. The factor names and physical meanings follow the established 15-factor CTM classification reported in Refs. [1–4].

2.6. Reliability, Qualification, and Diagnostics Framework

Qualification and reliability were assessed as an evidence framework rather than as a newly performed certification campaign. IEC 61215 [38] and IEC 61730 [39] define design-qualification and safety requirements, while IEC TS 60904-1-2 [40] and IEC 60891 [41] support bifacial I–V measurement and irradiance/temperature correction. The degradation synthesis covers PID, LID/LeTID, corrosion, encapsulant discoloration, delamination, cell cracking, interconnection fatigue, hot spots, and junction-box or bypass-diode anomalies [42–47]. Infrared thermography was considered a diagnostic method that should be interpreted together with I–V, electroluminescence, continuity, and visual-inspection evidence [45,47].

Mechanical defects can evolve from electrically weak microcracks into crack-separated or electrically inactive cell regions under repeated mechanical loading and environmental exposure [48,49]. Electroluminescence imaging is therefore valuable for locating electrically inactive regions, crack-separated cell fragments, and recombination-active defects that may not be evident from visual inspection alone [50]. Potential-induced degradation additionally depends on device polarity, interface structure, encapsulation, temperature, humidity, and sustained system voltage, including technology-dependent responses in n-type crystalline-silicon devices [51,52]. Representative field and thermal-image examples are presented in Figure 5.

2.7. Scope and Uncertainty

The orientation plots are normalized and therefore support comparison of profile shape rather than absolute annual energy yield. The parallel Si/Si results depend on the technology-specific rear irradiance, the experimentally measured individual-cell electrical characteristics, the common-voltage evaluation procedure, and the adopted normalization factor φ. The III–V/n-TOPCon results depend on the starting cell efficiencies, transmitted-

spectrum treatment, bonding-layer optical contribution, selected CTM sequence, and individual k_1–k_{15} factor values. Accordingly, the reported results should be used for comparative design analysis and physical-consistency assessment rather than as certified module ratings.

Wavelength-resolved external quantum efficiency (EQE) measurements were performed for the investigated PERC, TOPCon, HJT, and IBC silicon solar cells and are presented in Figure 6g. These measurements provide complementary spectral-response information to the J–V characteristics and support interpretation of the technology-dependent photocurrent behavior. However, for the III–V/n-TOPCon CTM configurations, configuration-specific EQE measurements of the silicon bottom cell under the spectrum transmitted through each corresponding top-cell stack were not independently performed. Therefore, the filtered-spectrum bottom-cell response in the III–V/n-TOPCon CTM analysis should continue to be interpreted according to the transmitted-spectrum assumptions described in Section 2.5.2.

3. Results

3.1. Architecture and Module-Integration Implications

Figure 1 demonstrates that the module-integration problem changes with the cell architecture. PERC and TOPCon retain front metallization but differ strongly in rear-passivating-contact structure, emitter configuration, firing compatibility, and contact formation [5,32–34]. HJT introduces transparent-conductive-oxide absorption and low-temperature interconnection constraints, making metallization and contact optimization particularly important [6,7,35]. IBC removes front-grid shading but introduces rear-contact alignment and lateral-current-transport complexity [6,36]. For mechanically stacked III–V/Si modules, optical transmission through the top device, bonding-stack transparency, spectral albedo, and the external terminal configuration directly govern the usable current and power of the silicon bottom cell [19,27–31].

The architecture classification in Figure 2 further shows that tandem integration is governed by both physical stacking and terminal design. Two-terminal monolithic configurations require current matching between subcells, whereas four-terminal arrangements permit independent electrical operation but require additional transparent contacts and external connections. Three-terminal and voltage-matched configurations provide intermediate design options, with performance determined by interface transparency, recombination layers, bonding quality, and electrical extraction [18–26].

3.2. Orientation-Dependent Bifacial Behavior

The normalized profiles in Figure 3 show distinct orientation-dependent generation patterns. The tilted and horizontal configurations concentrate output around solar noon. The vertical east–west configuration produces two broader peaks in the morning and afternoon, which may improve temporal matching with demand despite a lower midday maximum. Dual-axis tracking maintains a favorable incidence angle over a longer period and therefore produces the broadest high-output profile in the illustrative comparison. These trends are consistent with the dependence of bifacial output on front- and rear-side irradiance, albedo, module elevation, orientation, tracker geometry, and irradiance mismatch [13–17,37].

3.3. Reliability and Degradation Implications

Figure 4 links operating-time regimes with material, manufacturing, structural, and electrical failure pathways. Early losses may originate from stabilization, LID, LeTID, handling damage, or connection faults; mid-life losses increasingly involve PID, interconnect

fatigue, diode failure, and packaging defects; and wear-out is dominated by corrosion, cracking, and cumulative environmental exposure. Microcracks may initially cause only limited measurable power reduction but can develop into larger electrically isolated regions following cyclic loading or environmental aging [48,49]. In addition, degradation and recovery studies on HJT and mechanically stacked III–V/Si devices have investigated controlled AC-power application as a possible mitigation or regeneration approach under light- and elevated-temperature-induced degradation conditions [53,54]. The normalized V_{oc} trajectories illustrate that PERC, SHJ/HJT, and TOPCon technologies can exhibit substantially different stability responses. These trajectories are indicative and must be interpreted together with the specific stress protocol and supporting J_{sc}, FF, resistance, and imaging data [42–47].

3.4. Infrared Thermography and Field Diagnostics

Infrared thermography provides rapid, non-contact identification of abnormal thermal behavior in photovoltaic modules. Figure 5 illustrates localized heating under field and inspection conditions, ranging from moderate temperature nonuniformity to severe localized hot-spot behavior. Such thermal anomalies may be associated with electrical mismatch, partial shading, cell cracking, defective interconnections, bypass-diode malfunction, or increased local resistance. Infrared observations should therefore be evaluated together with current–voltage measurements, electroluminescence imaging, irradiance conditions, module operating state, and visual inspection [45,47]. In particular, electroluminescence imaging can complement infrared thermography by identifying crack-separated cell regions, electrically inactive areas, and spatially nonuniform recombinations that may not produce a distinct thermal signature under every operating condition [50].

3.5. Parallel-Coupled Si/Si Performance

Figure 6a–i summarizes the electrical and spectral characteristics of the parallel Si/Si configurations. Figure 6b–f presents J_{sc}, V_{oc}, FF, conversion efficiency, and maximum-power density for Cell 1, Cell 2, and the corresponding parallel-coupled configurations at their respective technology-specific maximum-output conditions. Figure 6g presents the wavelength-resolved EQE characteristics of the investigated PERC, TOPCon, HJT, and IBC silicon solar cells. Figure 6h shows the J–V characteristics of Cell 1, Cell 2, and the corresponding parallel-coupled configurations, while Figure 6i presents the corresponding P–V characteristics. The parallel electrical outputs were obtained by voltage-resolved, point-by-point current addition at a common operating voltage using Equations (8)–(11). Table 3 reports both the tandem efficiencies and the physical efficiencies calculated using the complete front-plus-rear incident power.

At the respective technology-specific maximum-output conditions, the HJT-based parallel Si/Si configuration produced the highest η_{tandem} of 32.43% and the highest $\eta_{physical}$ of 26.85%, followed by IBC with η_{tandem} = 32.29% and $\eta_{physical}$ = 26.65%. TOPCon reached η_{tandem} = 31.62% and $\eta_{physical}$ = 26.08%, whereas PERC reached η_{tandem} = 28.42% and $\eta_{physical}$ = 23.45%. However, these results do not constitute a fixed-rear-irradiance head-to-head comparison because the PERC maximum was obtained at a rear irradiance of 50 mW cm^{-2}, whereas the TOPCon, HJT, and IBC maxima were obtained at 40 mW cm^{-2}. The ranking should therefore be interpreted only within the technology-specific operating conditions investigated.

Table 3. Electrical performance of the parallel-coupled Si/Si configurations at their respective technology-specific maximum-output conditions.

Si/Si Tandem Technology	G_{rear} (mW cm^{-2})	$J_{sc,parallel}$ (mA cm^{-2})	$V_{oc,parallel}$ (V)	$FF_{parallel}$ (%)	P_{max}/A (mW cm^{-2})	φ, Rear-Side Utilization Factor	η_{tandem} (%)	$\eta_{physical}$ (%)
PERC	50	62.66	0.68	82.28	35.17	0.475	28.42	23.45
TOPCon	40	58.79	0.73	85.29	36.51	0.387	31.62	26.08
HJT	40	57.79	0.75	87.21	37.59	0.398	32.43	26.85
IBC	40	59.24	0.73	86.21	37.31	0.389	32.29	26.65

Note: G_{front} = 100 mW cm^{-2} for all configurations. The PERC maximum-output condition was obtained at G_{rear} = 50 mW cm^{-2}, whereas the TOPCon, HJT, and IBC maximum-output conditions were obtained at G_{rear} = 40 mW cm^{-2}. Therefore, the reported values represent technology-specific maximum-output conditions rather than a fixed-rear-irradiance comparison. The tandem efficiency, η_{tandem}, was calculated using the effective irradiance $G_{front} + \varphi G_{rear}$, whereas the physical total-input efficiency, $\eta_{physical}$, was calculated as $(P_{max}/A)/(G_{front} + G_{rear}) \times 100$. Accordingly, η_{tandem} should not be interpreted as an efficiency based on the complete front-plus-rear incident power. Maximum-power densities were calculated using unrounded electrical parameters; minor differences may occur when the values are recalculated using the rounded J_{sc}, V_{oc}, and FF values displayed in the table.

The parallel connection primarily increases the combined short-circuit current density through point-by-point current addition at a common operating voltage. The open-circuit voltage and fill factor remain dependent on the voltage compatibility and individual current–voltage characteristics of the coupled devices. The HJT- and IBC-based configurations maintained comparatively high fill factors under the examined conditions, whereas the PERC-based configuration exhibited the lowest η_{tandem} and $\eta_{physical}$ values. Both reporting bases are provided for transparency: η_{tandem} uses the adopted effective irradiance $G_{front} + \varphi G_{rear}$, whereas $\eta_{physical}$ accounts for the complete front-plus-rear incident power, $G_{front} + G_{rear}$, and is therefore used as the complete-input energy-accounting metric.

3.6. III–V/n-TOPCon CTM Performance

The factor-resolved III–V/n-TOPCon CTM results presented in Figure 6j are summarized in Table 4. Under the adopted CTM input conditions, the III–V Flex/n-TOPCon, GaAs type-1/n-TOPCon, and GaAs type-2/n-TOPCon configurations retained approximately 89.4% of their initial cell-level efficiencies after the complete factor sequence. GaAs type-2/n-TOPCon produced the highest resulting module efficiency of 31.16%, whereas GaAs type-1/n-TOPCon showed the lowest absolute CTM reduction of 3.24 percentage points.

Table 4. Initial cell efficiencies and resulting module efficiencies obtained from the factor-resolved III–V/n-TOPCon CTM analysis.

Configuration	Cell Efficiency (%)	Resulting Module Efficiency (%)	Absolute CTM Reduction (% Absolute)	Efficiency Retained (%)
III–V Flex/n-TOPCon	33.74	30.18	3.56	89.45
GaAs type-1/n-TOPCon	30.72	27.48	3.24	89.45
GaAs type-2/n-TOPCon	34.84	31.16	3.68	89.44

The waterfall plot shows that the largest individual penalties occur within the geometrical and optical-loss portions of the sequence, whereas the optical-gain terms *k8–k11* partially recover the lost efficiency. The result emphasizes that the highest starting cell efficiency does not automatically produce the smallest absolute CTM reduction.

4. Discussion

The comparative results demonstrate that photovoltaic modules must be evaluated as coupled optical, electrical, thermal, mechanical, and reliability systems. Cell architecture determines the available voltage, bifacial response, contact geometry, interconnection temperature, and susceptibility to optical or resistive loss. Module packaging can therefore either preserve or erode the advantages achieved at the cell level. Accordingly, passivating-contact formation, emitter design, metallization, back-contact geometry, and low-temperature interconnection must be optimized according to the specific requirements of TOPCon, HJT, and IBC technologies rather than applying a single module-integration strategy to all cell types [8–12,32–36].

From a practical module-design and manufacturing perspective, technology selection should be based not only on standalone cell efficiency but also on architecture-specific integration compatibility. TOPCon module optimization should prioritize preservation of the passivating contact, firing compatibility, metallization resistance, and rear-side optical management. HJT module manufacturing requires low-temperature interconnection, stable TCO/contact interfaces, and moisture-resistant packaging. IBC modules require precise rear-contact alignment, low-resistance lateral current transport, and appropriate rear-side inspection procedures. For bifacial and tandem modules, mounting geometry, rear-irradiance conditions, optical-interlayer transmission, terminal configuration, and subcell operating-voltage compatibility should be considered together before the module design is finalized.

The parallel Si/Si analysis demonstrates why the irradiance denominator and rear-side utilization convention must be stated explicitly. Values of η_{tandem} exceeding 32% were obtained using the effective irradiance $G_{front} + \varphi G_{rear}$, whereas the corresponding $\eta_{physical}$ values based on the complete front-plus-rear incident power were approximately 23–27%. These values are not contradictory because η_{tandem} and $\eta_{physical}$ use different irradiance denominators. However, because the effective rear-side utilization factors were back-calculated from the reported maximum-power densities and original η_{tandem} values, η_{tandem} should be interpreted as a convention-dependent comparative metric rather than an independently measured complete-input efficiency. The $\eta_{physical}$ metric accounts for the complete front-plus-rear incident power and therefore provides the appropriate basis for energy-conservation assessment and comparison among independently illuminated photovoltaic configurations.

The parallel Si/Si arrangement is not a conventional spectral tandem. Its gain is produced by separate optical inputs and current addition at a common voltage. By contrast, III–V/Si and perovskite/Si tandems rely on spectral division, so the silicon bottom cell must be evaluated under the spectrum transmitted through the top stack [18–26]. Treating both subcells as independently illuminated by the full one-sun spectrum would double-count the optical input. The appropriate treatment additionally depends on terminal configuration because two-terminal tandems impose subcell-matching constraints, whereas three- and four-terminal configurations permit different degrees of electrical independence at the cost of increased contact and interconnection complexity [27–31].

Reliability remains a separate bankability constraint. Qualification tests provide evidence against defined stress sequences but do not reproduce every climate, mechanical-load, system-voltage, or field interaction. Microcracking can develop progressively under cyclic mechanical and environmental loading, while PID behavior is influenced by cell polarity, interface structure, encapsulation, humidity, temperature, and applied voltage [48,49,51,52]. PID, LeTID, corrosion, cracking, hot spots, and interconnection failure can produce similar power-loss signatures; diagnosis should therefore combine I–V analysis, electroluminescence, infrared thermography, visual inspection, and installation metadata [38–47,50].

Recovery-oriented studies on HJT and mechanically stacked III–V/Si devices further indicate that electrical excitation history should be considered when interpreting degradation and regeneration behavior [53,54]. The localized thermal anomalies shown in Figure 5 consequently illustrate why infrared inspection is most informative when interpreted together with electrical and complementary imaging evidence rather than as a standalone diagnostic method.

The principal limitation of this study is that the bifacial-orientation curves and reliability framework are normalized comparative syntheses rather than site-specific energy-yield predictions or certification datasets. The parallel Si/Si maximum-output conditions were obtained using different rear irradiances, with 50 mW cm^{-2} applied to the PERC configuration and 40 mW cm^{-2} applied to the TOPCon, HJT, and IBC configurations. Consequently, the reported maxima should not be interpreted as a fixed-condition technology ranking. In addition, the effective rear-side weighting coefficients were back-calculated rather than independently measured, and the factor-resolved III–V/n-TOPCon CTM results depend on the adopted starting efficiencies, filtered-spectrum treatment, bonding-layer transmission, k_1–k_{15} factor sequence, and individual efficiency-change values. The present analysis also does not include a complete uncertainty budget covering all experimental and CTM input parameters. Future work should validate the framework through controlled module fabrication, independently measured bifaciality factors, uniform front- and rear-side irradiance, configuration-specific filtered-spectrum EQE measurements for the III–V/n-TOPCon bottom cells, measured top-stack spectral transmission and bonding-layer optical properties, clearly defined CTM factor values, uncertainty propagation, and long-term outdoor monitoring.

5. Conclusions

This study established a common module-level framework linking solar-cell architecture, bifacial orientation, parallel electrical coupling, CTM conversion, degradation, and diagnostic assessment. The comparison demonstrates that module output cannot be predicted from standalone cell efficiency alone because manufacturing compatibility, rear irradiance, operating-voltage matching, inactive area, optical coupling, spectral transmission, and electrical-interconnection losses must be considered together. At the respective technology-specific maximum-output conditions, the parallel Si/Si configurations reached η_{tandem} values of 28.42% for PERC, 31.62% for TOPCon, 32.43% for HJT, and 32.29% for IBC. When the complete front-plus-rear incident power was considered, the corresponding $\eta_{physical}$ values were 23.45%, 26.08%, 26.85%, and 26.65%. Because the configurations were evaluated at different rear irradiances and the rear-side utilization factors were not independently measured, these results should be interpreted under the adopted technology-specific operating and normalization conditions rather than as a fixed-condition technology ranking. Within the examined conditions, the HJT-based configuration provided the highest performance on both reporting bases. The factor-resolved III–V/n-TOPCon CTM analysis yielded resulting module efficiencies of 30.18%, 27.48%, and 31.16% for the III–V Flex/n-TOPCon, GaAs type-1/n-TOPCon, and GaAs type-2/n-TOPCon configurations, respectively, corresponding to calculated absolute CTM reductions of 3.56, 3.24, and 3.68 percentage points. Transparent irradiance definitions, consistent η_{tandem} normalization, complete-input $\eta_{physical}$ reporting, and factor-resolved CTM accounting are therefore essential for the fair comparison of emerging photovoltaic module architectures.

Author Contributions: Conceptualization, H.Y. and J.Y.; methodology, H.Y., R.U.R., A., M.C., M.N.A., S.A.M., X.W., H.J. and M.Q.K.; formal analysis, H.Y.; validation, all authors; investigation, H.Y., R.U.R. and M.Q.K.; data curation, H.Y.; writing—original draft preparation, H.Y.; writing—review

and editing, all authors; visualization, H.Y.; supervision, J.Y.; project administration, J.Y.; funding acquisition, J.Y. All authors have read and agreed to the published version of the manuscript.

Funding: This work was supported by the Korea Institute of Energy Technology Evaluation and Planning (KETEP) and the Ministry of Climate, Energy and Environment (MCEE) of the Republic of Korea (Grant Nos. RS-2026-25536152 and RS-2025-25444655).

Data Availability Statement: The data supporting the findings of this study are available from the corresponding author upon reasonable request.

Conflicts of Interest: The authors declare no conflicts of interest.

Abbreviations

AM1.5G, air mass 1.5 global; c-Si, crystalline silicon; CTM, cell-to-module; DHI, diffuse horizontal irradiance; DNI, direct normal irradiance; EL, electroluminescence; FF, fill factor; GHI, global horizontal irradiance; HJT, heterojunction; IBC, interdigitated back contact; III–V, group III–V semiconductor; IR, infrared; Jsc, short-circuit current density; LID, light-induced degradation; LeTID, light- and elevated-temperature-induced degradation; MPP, maximum power point; PERC, passivated emitter and rear cell; PID, potential-induced degradation; Pmax, maximum electrical power; PV, photovoltaic; SHJ, silicon heterojunction; STC, standard test conditions; TCO, transparent conductive oxide; TOPCon, tunnel-oxide passivated contact; Voc, open-circuit voltage.

References

1. Mittag, M.; Zech, T.; Wiese, M.; Blasi, D.; Ebert, M.; Wirth, H. Cell-to-Module (CTM) Analysis for Photovoltaic Modules with Shingled Solar Cells. In *Proceedings of the 2017 IEEE 44th Photovoltaic Specialist Conference (PVSC)*; IEEE: Piscataway, NJ, USA, 2017; pp. 1531–1536.
2. Haedrich, I.; Eitner, U.; Wiese, M.; Wirth, H. Unified methodology for determining CTM ratios: Systematic prediction of module power. *Sol. Energy Mater. Sol. Cells* **2014**, *131*, 14–23. [CrossRef]
3. Hanifi, H.; Pfau, C.; Turek, M.; Schneider, J. A practical optical and electrical model to estimate the power losses and quantification of different heat sources in silicon-based PV modules. *Renew. Energy* **2018**, *127*, 602–612. [CrossRef]
4. Jung, T.H.; Lee, J.I.; Song, H.E.; Ju, Y.C.; Ko, S.W.; Jung, Y.S.; Kang, G.H. Classification conditions of cells to reduce cell-to-module conversion loss at the production stage of PV modules. *Renew. Energy* **2017**, *103*, 582–593. [CrossRef]
5. Feldmann, F.; Bivour, M.; Reichel, C.; Steinkemper, H.; Hermle, M.; Glunz, S.W. Tunnel oxide passivated contacts as an alternative to partial rear contacts. *Sol. Energy Mater. Sol. Cells* **2014**, *131*, 46–50. [CrossRef]
6. Yoshikawa, K.; Kawasaki, H.; Yoshida, W.; Irie, T.; Konishi, K.; Nakano, K.; Uto, T.; Adachi, D.; Kanematsu, M.; Uzu, H.; et al. Silicon heterojunction solar cell with interdigitated back contacts for a photoconversion efficiency over 26%. *Nat. Energy* **2017**, *2*, 17032. [CrossRef]
7. Taguchi, M.; Yano, A.; Tohoda, S.; Matsuyama, K.; Nakamura, Y.; Nishiwaki, T.; Fujita, K.; Maruyama, E. 24.7% record efficiency HIT solar cell on thin silicon wafer. *IEEE J. Photovolt.* **2014**, *4*, 96–99. [CrossRef]
8. Richter, A.; Hermle, M.; Glunz, S.W. Reassessment of the limiting efficiency for crystalline silicon solar cells. *IEEE J. Photovolt.* **2013**, *3*, 1184–1191. [CrossRef]
9. Masuko, K.; Shigematsu, M.; Hashiguchi, T.; Fujishima, D.; Kai, M.; Yoshimura, N.; Yamaguchi, T.; Ichihashi, Y.; Mishima, T.; Matsubara, N.; et al. Achievement of more than 25% conversion efficiency with crystalline silicon heterojunction solar cell. *IEEE J. Photovolt.* **2014**, *4*, 1433–1435. [CrossRef]
10. Adachi, D.; Hernández, J.L.; Yamamoto, K. Impact of carrier recombination on fill factor for large-area heterojunction crystalline silicon solar cell with 25.1% efficiency. *Appl. Phys. Lett.* **2015**, *107*, 233506. [CrossRef]
11. Tomasi, A.; Paviet-Salomon, B.; Jeangros, Q.; Haschke, J.; Christmann, G.; Barraud, L.; Descoeudres, A.; Seif, J.P.; Nicolay, S.; Despeisse, M.; et al. Simple processing of back-contacted silicon heterojunction solar cells using selective-area crystalline growth. *Nat. Energy* **2017**, *2*, 17062. [CrossRef]
12. Liu, W.; Shi, J.; Zhang, L.; Han, A.; Huang, S.; Li, X.; Peng, J.; Yang, Y.; Gao, Y.; Yu, J.; et al. Light-induced activation of boron doping in hydrogenated amorphous silicon for over 25% efficiency silicon solar cells. *Nat. Energy* **2022**, *7*, 427–437. [CrossRef]
13. Deline, C.; MacAlpine, S.; Marion, B.; Toor, F.; Asgharzadeh, A.; Stein, J.S. Assessment of bifacial photovoltaic module power rating methodologies—Inside and out. *IEEE J. Photovolt.* **2017**, *7*, 575–580. [CrossRef]
14. Deline, C.; Ayala Pelaez, S.; MacAlpine, S.; Olalla, C. Estimating and parameterizing mismatch power loss in bifacial photovoltaic systems. *Prog. Photovolt. Res. Appl.* **2020**, *28*, 691–703. [CrossRef]

15. Sun, X.; Khan, M.R.; Deline, C.; Alam, M.A. Optimization and performance of bifacial solar modules: A global perspective. *Appl. Energy* **2018**, *212*, 1601–1610. [CrossRef]
16. Ayala Pelaez, S.; Deline, C.; Greenberg, P.; Stein, J.S.; Kostuk, R.K. Model and validation of single-axis tracking with bifacial PV. *IEEE J. Photovolt.* **2019**, *9*, 715–721. [CrossRef]
17. Rodríguez-Gallegos, C.D.; Liu, H.; Gandhi, O.; Singh, J.P.; Krishnamurthy, V.; Kumar, A.; Stein, J.S.; Wang, S.; Li, L.; Reindl, T.; et al. Global techno-economic performance of bifacial and tracking photovoltaic systems. *Joule* **2020**, *4*, 1514–1541. [CrossRef]
18. Sahli, F.; Werner, J.; Kamino, B.A.; Bräuninger, M.; Monnard, R.; Paviet-Salomon, B.; Barraud, L.; Ding, L.; Diaz Leon, J.J.; Sacchetto, D.; et al. Fully textured monolithic perovskite/silicon tandem solar cells with 25.2% power conversion efficiency. *Nat. Mater.* **2018**, *17*, 820–826. [CrossRef]
19. Essig, S.; Allebé, C.; Remo, T.; Geisz, J.F.; Steiner, M.A.; Horowitz, K.; Barraud, L.; Ward, J.S.; Schnabel, M.; Descoeudres, A.; et al. Raising the one-sun conversion efficiency of III–V/Si solar cells to 32.8% for two junctions and 35.9% for three junctions. *Nat. Energy* **2017**, *2*, 17144. [CrossRef]
20. Geisz, J.F.; France, R.M.; Schulte, K.L.; Steiner, M.A.; Norman, A.G.; Guthrey, H.L.; Young, M.R.; Song, T.; Moriarty, T. Six-junction III–V solar cells with 47.1% conversion efficiency under 143 suns concentration. *Nat. Energy* **2020**, *5*, 326–335. [CrossRef]
21. Al-Ashouri, A.; Köhnen, E.; Li, B.; Magomedov, A.; Hempel, H.; Caprioglio, P.; Márquez, J.A.; Morales Vilches, A.B.; Kasparavičius, E.; Smith, J.A.; et al. Monolithic perovskite/silicon tandem solar cell with >29% efficiency by enhanced hole extraction. *Science* **2020**, *370*, 1300–1309.
22. Aydin, E.; Ugur, E.; Yildirim, B.K.; De Bastiani, M.; Allen, T.G.; Khenkin, M.V.; Cao, Y.; Xu, L.; Isikgor, F.H.; Soltanpoor, W.; et al. Enhanced optoelectronic coupling for perovskite/silicon tandem solar cells. *Nature* **2023**, *623*, 732–738. [CrossRef]
23. Liu, J.; Aydin, E.; Yin, J.; De Bastiani, M.; Isikgor, F.H.; Rehman, A.U.; Yengel, E.; Ugur, E.; Harrison, G.T.; Wang, M.; et al. Perovskite/silicon tandem solar cells with bilayer interface passivation. *Nature* **2024**, *635*, 596–603. [CrossRef]
24. Artuk, K.; Oranskaia, A.; Turkay, D.; Saenz, F.; Mensi, M.D.; De Bastiani, M.; Castro-Méndez, A.-F.; Hurni, J.; Allebé, C.; Othman, M.; et al. 60 cm^2 perovskite–silicon tandem solar cells with an efficiency of 28.9% by homogeneous passivation. *Nat. Commun.* **2025**, *16*, 8672. [CrossRef]
25. Xu, L.; Liu, J.; Toniolo, F.; Isikgor, F.H.; De Bastiani, M.; Allen, T.G.; Ugur, E.; Yildirim, B.K.; Harrison, G.T.; Aydin, E.; et al. Monolithic perovskite/silicon tandem photovoltaics with minimized cell-to-module losses by refractive-index engineering. *ACS Energy Lett.* **2022**, *7*, 2370–2372. [CrossRef]
26. Babics, M.; De Bastiani, M.; Ugur, E.; Xu, L.; Bristow, H.L.; Toniolo, F.; Raja, W.; Subbiah, A.S.; Liu, J.; Torres Merino, L.V.; et al. One-year outdoor operation of monolithic perovskite/silicon tandem solar cells. *Cell Rep. Phys. Sci.* **2023**, *4*, 101280. [CrossRef]
27. Schulte-Huxel, H.; Friedman, D.J.; Tamboli, A.C. String-level modeling of two-, three-, and four-terminal Si-based tandem modules. *IEEE J. Photovolt.* **2018**, *8*, 1370–1375. [CrossRef]
28. Cariou, R.; Benick, J.; Feldmann, F.; Höhn, O.; Hauser, H.; Beutel, P.; Razek, N.; Wimplinger, M.; Bläsi, B.; Lackner, D.; et al. III–V-on-silicon solar cells reaching 33% photoconversion efficiency in two-terminal configuration. *Nat. Energy* **2018**, *3*, 326–333. [CrossRef]
29. Werner, J.; Barraud, L.; Walter, A.; Bräuninger, M.; Sahli, F.; Sacchetto, D.; Tétreault, N.; Paviet-Salomon, B.; Moon, S.J.; Allebé, C.; et al. Efficient near-infrared-transparent perovskite solar cells enabling direct comparison of four-terminal and monolithic perovskite/silicon tandem cells. *ACS Energy Lett.* **2016**, *1*, 474–480. [CrossRef]
30. Bush, K.A.; Palmstrom, A.F.; Yu, Z.J.; Boccard, M.; Cheacharoen, R.; Mailoa, J.P.; McMeekin, D.P.; Hoye, R.L.Z.; Bailie, C.D.; Leijtens, T.; et al. 23.6%-efficient monolithic perovskite/silicon tandem solar cells with improved stability. *Nat. Energy* **2017**, *2*, 17009. [CrossRef]
31. Alamgeer; Madara, P.C.; Khokhar, M.Q.; Yousuf, H.; Jony, J.A.; Rahman, R.U.; Bae, J.; Jang, S.; Shin, M.-K.; Park, S.; et al. Enhanced Bifacial III–V/Silicon Multijunction Solar-Cell-Based Promising Structure of c-Si Bottom Cells. *ACS Appl. Energy Mater.* **2025**, *8*, 991–997. [CrossRef]
32. Rahman, R.U.; Khokhar, M.Q.; Yousuf, H.; Aida, M.N.; Jony, J.A.; Madara, P.C.; Chu, M.; Park, S.; Yi, J. Optimization Strategies for Metallization in N-Type Crystalline Silicon TOPCon Solar Cells: Pathways to Elevated Fill Factor and Enhanced Efficiency. *Curr. Appl. Phys.* **2024**, *67*, 107–114. [CrossRef]
33. Alamgeer; Khokhar, M.Q.; Yousuf, H.; Dao, V.-A.; Bae, J.; Kim, E.H.; Park, S.; Pham, D.P.; Yi, J. Tunnel Silicon Oxynitride Phase Transformation for N-Type Polysilicon Passivating Contacts in Crystalline Silicon Solar Cells. *Inorg. Chem. Commun.* **2024**, *170*, 113282. [CrossRef]
34. Khokhar, M.Q.; Yousuf, H.; Alamgeer; Chu, M.; Rahman, R.U.; Aida, M.N.; Mohammed, S.A.; Wang, X.; Yi, J. Design and Optimization of Emitter Configurations for High-Efficiency P-Type Tunnel Oxide Passivated Contact Solar Cells. *Energy Technol.* **2026**, *14*, e202501437. [CrossRef]
35. Alamgeer; Aida, M.N.; Khokhar, M.Q.; Yousuf, H.; Tariq, A.; Zahid, M.A.; Park, S.; Yi, J. Metallization Process Optimization of HIT Solar Cell for High Current Density and Silver Reduction. *Inorg. Chem. Commun.* **2024**, *170*, 113480. [CrossRef]

36. Khokhar, M.Q.; Yousuf, H.; Alamgeer; Chu, M.; Ur Rahman, R.; Jony, J.A.; Qamar Hussain, S.; Pham, D.P.; Yi, J. Systematic Modeling and Optimization for High-Efficiency Interdigitated Back-Contact Crystalline Silicon Solar Cells. *Energy Technol.* **2024**, *12*, 2400831. [CrossRef]
37. Ayala Pelaez, S.; Deline, C. bifacial_radiance: A Python package for modeling bifacial solar photovoltaic systems. *J. Open Source Softw.* **2020**, *5*, 1865. [CrossRef]
38. *IEC 61215-2:2021*; Terrestrial Photovoltaic (PV) Modules—Design Qualification and Type Approval—Part 2: Test Procedures. International Electrotechnical Commission: Geneva, Switzerland, 2021.
39. *IEC 61730-1:2023*; Photovoltaic (PV) Module Safety Qualification—Part 1: Requirements for Construction. International Electrotechnical Commission: Geneva, Switzerland, 2023.
40. *IEC TS 60904-1-2:2024*; Photovoltaic Devices—Part 1–2: Measurement of Current–Voltage Characteristics of Bifacial Photovoltaic Devices. International Electrotechnical Commission: Geneva, Switzerland, 2024.
41. *IEC 60891:2021*; Photovoltaic Devices—Procedures for Temperature and Irradiance Corrections to Measured I–V Characteristics. International Electrotechnical Commission: Geneva, Switzerland, 2021.
42. Naumann, V.; Lausch, D.; Hähnel, A.; Bauer, J.; Breitenstein, O.; Graff, A.; Werner, M.; Swatek, S.; Hagendorf, C. Explanation of potential-induced degradation of the shunting type by Na decoration of stacking faults in Si solar cells. *Sol. Energy Mater. Sol. Cells* **2014**, *120*, 383–389. [CrossRef]
43. Kersten, F.; Engelhart, P.; Ploigt, H.C.; Stekolnikov, A.; Lindner, T.; Stenzel, F.; Bartzsch, M.; Szpeth, A.; Petter, K.; Heitmann, J.; et al. Degradation of multicrystalline silicon solar cells and modules after illumination at elevated temperature. *Sol. Energy Mater. Sol. Cells* **2015**, *142*, 83–86. [CrossRef]
44. Kyranaki, N.; Smith, A.; Yendall, K.; Hutt, D.A.; Whalley, D.C.; Gottschalg, R.; Betts, T.R. Damp-heat-induced degradation in photovoltaic modules manufactured with passivated emitter and rear contact solar cells. *Prog. Photovolt. Res. Appl.* **2022**, *30*, 1061–1071. [CrossRef]
45. Gallardo-Saavedra, S.; Hernández-Callejo, L.; Alonso-García, M.C.; Muñoz-Cruzado-Alba, J.; Ballestín-Fuertes, J. Infrared thermography for the detection and characterization of photovoltaic defects: Comparison between illumination and dark conditions. *Sensors* **2020**, *20*, 4395. [CrossRef]
46. Jordan, D.C.; Silverman, T.J.; Sekulic, B.; Kurtz, S.R. PV degradation curves: Non-linearities and failure modes. *Prog. Photovolt. Res. Appl.* **2017**, *25*, 583–591. [CrossRef]
47. Ahsan, S.; Niazi, K.A.K.; Khan, H.A.; Yang, Y. Hotspots and performance evaluation of crystalline-silicon and thin-film photovoltaic modules. *Microelectron. Reliab.* **2018**, *88–90*, 1014–1018. [CrossRef]
48. Paggi, M.; Berardone, I.; Infuso, A.; Corrado, M. Fatigue degradation and electric recovery in silicon solar cells embedded in photovoltaic modules. *Sci. Rep.* **2014**, *4*, 4506. [CrossRef]
49. Köntges, M.; Kunze, I.; Kajari-Schröder, S.; Breitenmoser, X.; Bjørneklett, B. The risk of power loss in crystalline silicon-based photovoltaic modules due to microcracks. *Sol. Energy Mater. Sol. Cells* **2011**, *95*, 1131–1137. [CrossRef]
50. Fuyuki, T.; Kondo, H.; Yamazaki, T.; Takahashi, Y.; Uraoka, Y. Photographic surveying of minority-carrier diffusion length in polycrystalline silicon solar cells by electroluminescence. *Appl. Phys. Lett.* **2005**, *86*, 262108. [CrossRef]
51. Bauer, J.; Naumann, V.; Großer, S.; Hagendorf, C.; Schütze, M.; Breitenstein, O. On the mechanism of potential-induced degradation in crystalline silicon solar cells. *Phys. Status Solidi RRL* **2012**, *6*, 331–333. [CrossRef]
52. Hara, K.; Jonai, S.; Masuda, A. Potential-induced degradation in photovoltaic modules based on n-type single-crystalline silicon solar cells. *Sol. Energy Mater. Sol. Cells* **2015**, *140*, 361–365. [CrossRef]
53. Rahman, R.U.; Jony, J.A.; Alamgeer; Yousuf, H.; Khokhar, M.Q.; Aida, M.N.; Mohammed, S.A.; Park, S.; Yi, J. Enhancing regeneration and long-term reliability of c-Si (HIT) solar cells through AC power application for light- and elevated-temperature-induced degradation mitigation. *J. Renew. Sustain. Energy* **2025**, *17*, 043507. [CrossRef]
54. Jony, J.A.; Madara, P.C.; Yousuf, H.; Chu, M.; Alamgeer; Rahman, R.U.; Bae, J.; Jang, S.; Aida, M.N.; Sanyal, S.; et al. Improved ac square wave-based mitigation technique for III-V/Si Bi-facial tandem solar cells under stress caused by light and elevated temperature induced degradation. *Mater. Sci. Semicond. Process.* **2025**, *194*, 109540. [CrossRef]

Disclaimer/Publisher's Note: The statements, opinions and data contained in all publications are solely those of the individual author(s) and contributor(s) and not of MDPI and/or the editor(s). MDPI and/or the editor(s) disclaim responsibility for any injury to people or property resulting from any ideas, methods, instructions or products referred to in the content.